

Polyvinylimidazole-wrapped Halloysite Nanotubes for High Proton Conductivity in Polymer Electrolyte Membranes

Xiaoyang Liu¹, Xiang Sun, Hongqian Ren, Mengjie Yang, Mingling Xia, Jinghe Hou*, Yi Feng*, Huili Ding*

Institute of Polymer Science and Engineering, School of Chemical Engineering and Technology, Hebei University of Technology, Tianjin 300130, PR China

*E-mail: aleeding@hebut.edu.cn, 741925221@qq.com, yvonne.f512@gmail.com

Received: 20 December 2019 / *Accepted:* 6 August 2020 / *Published:* 31 August 2020

The construction of continuous proton transfer channels within a proton exchange membrane is an important and challenging task for the logical design of proton exchange membranes. Herein, inspired by the mechanism of moisture transport used by plants and biological proton transfer, polyvinylimidazole-wrapped halloysite nanotubes were proposed as proton carriers and nanochannels to afford polymer electrolyte membranes with high proton conductivities. The composite membranes were constructed by mixing sulfonated poly(aryl ether sulfone) (SPES) matrix and polyvinylimidazole-wrapped halloysite nanotubes (PVI@HNTs), PVI@HNTs were prepared by distillation-precipitation polymerization among them. Through a comprehensive study on the microstructure, physical and chemical properties and proton conductivity of the composite membrane, it was found that well-dispersed PVI @HNTs improved the mechanical and thermal stability of the nanocomposite membrane. The sulfonic acid groups in the polymer matrix formed acid-base pairs with the imidazolyl groups of the PVI@HNTs, which formed proton hopping pathways and nanochannels with low energy barriers for proton transfer. In addition, similar to plant ducts, one-dimensional and large aspect ratio tubular structures provided rapid transport channels for moisture in the membrane. The combination of "vehicle mechanism" and "Grotes mechanism" has significantly improved the proton conductivity of the SPES / PVI @ HNTs-X composite membrane. Specifically, the proton conductivity of 0.198 S cm⁻¹ at 80°C was obtained for SPES/PVI@HNTs-7.5 membrane, which was 46% higher than that of SPES. This research could provide a general and simple strategy to design composite exchange membranes.

Keywords: Halloysite nanotubes, nanocomposite membranes, proton transport channels, polyvinylimidazole-wrapped halloysite nanotubes, proton exchange membrane

1. INTRODUCTION

Proton exchange membrane fuel cells (PEMFCs) are hopeful candidates among the partial substitution of fossil fuel energy in recent years because of their excellent advantages, for example,

environmental friendliness and high energy efficiency [1-3]. In PEMFC, protons are transported from one side of the proton exchange membrane (PEM) to the other, through the transfer of the anode to the cathode, thereby performing energy conversion and providing electrical energy for the device. As a result of this, the PEM is an important part of a PEMFC, and it is often the performance-limiting component [4]. The most representative and most widely used proton exchange membrane material that has been used commercially in PEMFCs is the Nafion[®] series of membranes developed by DuPont in the United States. These membranes have both a hydrophobic polytetrafluoroethylene skeleton and branched chains with hydrophilic sulfonic acid groups, and they have high thermochemical stability and mechanical strength [5-7]. However, some of the shortcomings of such materials (for example, their fuel crossover and high cost), limit their broad application [8]. Therefore, the design and fabrication of alternative PEMs is crucial to the commercial application of PEMFCs [3].

Among all the materials that have been explored to synthesis PEMs, Sulfonated aromatic polymers are commonly used as a substitute for Nafion membranes, such as poly (aryl ether sulfone) (SPES) [9-11]. However, the “trade-off” effect of mechanical properties and the ionic conductivity limits the application of such membranes [12,13]. On the other hand, sulfonated aromatic polymer membranes display narrower proton channels and a greater number of “blind angle”, which reduce the completeness of the ion transfer channels [14]. The design and preparation of nanostructured composite membranes is considered as one of the effective strategies to conquer this challenge. In particular, a wide variety of multifunctional nanomaterials can be synthesized by different methods to provide flexible control of the interface microenvironment to achieve synergistic effects [12]. In recent years, researchers have paid great attention to how to synthesize membranes with continuous and sequential proton transport nanochannels. Due to the local accumulation of ionic groups, a tightly bonded hydrogen water structure or bond and network structure is formed in the nanochannel, resulting in high proton mobility [15-17]. Zhou et al. [18] showed that the proton conductivity increased by 50% when the content of sulfonated CNTs increases to 1.5 wt % in sulfonated poly(ether sulfone ether ketone ketone) (SPESEKK). He et al. [19] mixed CNTs functionalized with various groups (-COOH, -PO₃H₂, and -SO₃H) with a Nafion matrix to prepare composite membranes. Studies have shown that the proton conductivity of the membrane doped with 5% PCNT is significantly higher than that of Nafion at 100% RH. The continuous proton transmission path constructed by PCNT can significantly improve the proton conductivity of the membrane. He et al. [20] inspired by a nacre structure, used sulfonated polyvinyl alcohol as the matrix to prepare a 2D fast proton conduction channel proton exchange membrane by doping graphene oxide and montmorillonite. The MMT / SPVA-60 membrane with a large number of sulfonic acid groups and continuous 2D channels has a proton conductivity of 364 mS cm⁻¹ at 80 °C when fully hydrated. While, for composite PEMs containing CNTs and GO, high electron conductivity remains a major concern as it can result short circuits. Moreover, the costs of CNTs and GO are still fairly high [21].

The halloysite nanotubes (HNTs) are multilayered tubular aluminosilicate clay minerals (Al₂Si₂O₅(OH)₄ · 2H₂O) formed by natural kaolin curling, and they are Earth-abundant [22-24]. Compared with isotropic particles, HNT not only has an appropriate aspect ratio, large surface area, but also has excellent strength, easy dispersion in the matrix, facile introduction of new groups and natural availability. Since HNT has a good dispersion in the polymer matrix, it can form a filler

network that improves the thermal and mechanical properties of the material [25]. In addition, HNTs are more conducive to the construction of remotely ordered proton transfer channels. Recently, HNTs were used in composite PEM manufacturing [3,7,21,26]. Zhang et al. [3,7] mixed sulfonated HNTs and dopamine-modified HNTs with SPEEK to prepare composite membranes. The SPEEK-based membrane increases the proton conductivity due to the addition of modified HNT. Bai et al. [26] used CS as the matrix of the membrane and added a sulfonate-containing polyelectrolyte brush (SHNT) to construct a wide and continuous channel to increase the proton transport rate by the Grotthuss mechanism. However, the surface grafting rates of functionalized HNTs reported to date are not high, which may be for the hydroxyl group is mainly located in the lumen of HNT, and therefore, most of the groups grafted onto the HNTs will only be present in the lumen of the HNTs [21]. Therefore, in order to improve proton conductivity, it is very important to facilitate the construction of continuous proton transfer channel in the membrane. A new method of functionalizing the HNTs must be designed.

Various natural systems could inspire the fabrication of new proton exchange membrane materials [27,28]. Water and inorganic nutrients are transported in plants through the transport of tissue, and tubular cells are an ordered long-distance pathway for plant nutrients transport [29]. In biological proton transport, imidazole groups are a common motif, which are found in histidine residues. Such as protons are released from the cell by in imidazole group within hundreds of microseconds in the influenza A virus's M2 channel. Furthermore, an imidazole group can distort water molecules into either trigonal or tetrahedral geometries to form stable, one-dimensional water chain structures in many biological systems. Water can form continuous networks structure where protons can hop by this way [31]. Therefore, constructing a tubular, one-dimensional, highly efficient proton transport channel in a composite membrane using imidazole groups is anticipated to effectively enhance the proton conductivity of PEM.

In recent years, inspired by the mechanism of biological proton transfer, the halloysite nanotubes (PVI @ HNTs) coated with polyvinylimidazole were designed and synthesized in the light of plant water transport channels. Because the degree of sulfonation could be controlled, Sulfonated poly(aryl ether sulfone) (SPES) was prepared as a matrix, which synthesised by a nucleophilic polycondensation reaction and this material provides high strength and is low cost. Mixed the SPES matrix with PVI@HNTs and HNTs separately to prepare composite membranes (SPES/PVI@HNTs-X and SPES/HNTs-X), and the SPES/HNTs-X composite membrane was used as a control membrane. The membrane's microstructure and physical and chemical property were studied in detail. Through comparative tests with different membranes, their membrane water absorption, area expansion, ion-exchange capacity (IEC), thermal properties, mechanical strength and proton conductivity were detailed described. In addition, the proton migration mechanism of the SPES/PVI@HNTs-X membranes is discussed.

2. EXPERIMENTAL

2.1. Materials and chemicals

Halloysite nanotubes (HNTs) (Guangzhou Runwo Materials Technology Co., Ltd.), Vinylimidazole (VI) and 3-(Methacryloxy) propyltrimethoxysilane (MPS) (Alfa Aesar), 2,2'-Azobisisobutyronitrile (AIBN), methacrylic acid (MAA), ethylene glycol dimethacrylate (EGDMA), and tetramethylene sulfone (TMS) (Shanghai D&B Science and Technology Co., Ltd.), 4,4'-Difluorodiphenylsulfone (DFDPS) (Aladdin Reagent), according to a previous report, 3,3'-Disulfonate-4,4'-difluorodiphenylsulfone (SDFDPS) was synthesized from DCDPS [32]. Acetonitrile and N,N-Dimethylformamide (DMF) (Tianjin Jiangtian Chemical Technology Co., Ltd.), 4,4'-oxydiphenol (ODP) (Aladdin Reagent).

2.2. Preparation of polyvinylimidazole-wrapped halloysite nanotubes (PVI@HNTs)

The synthesis of PVI@HNTs is illustrated in Scheme 1. According to the previously reported methods, MPS-modified HNTs were prepared [26]; HNTs (10.0 g) were dispersed into a mixture of water (20 mL), aqueous ammonium (15 mL) and ethanol (180 mL) with stirring rapidly at room temperature for 24 h. After that, the reaction mixed with MPS (2.0 mL), and it was stirred for another 24 h. After three cycles of centrifugation, the MPS-modified HNTs have been purified, and next vacuum dried at 50 °C.

PVI@HNTs was synthesized by distillation and precipitation polymerization [4]. The synthesis steps of PVI@HNT are as follows: Mixed MPS-modified HNTs (0.30 g), AIBN (0.0216 g, 2 wt% relative to the comonomers), VI (0.5815 g), and the crosslinker (EGDMA, 0.5 g), with acetonitrile (80 mL) in a flask equipped with distillation and condensation device. The mixture was heated to boiling, and after the 40 mL of acetonitrile solvent was removed by distillation, the reaction was stopped. By three cycles of ultracentrifugation, decanting, and resuspension, the PVI@HNTs were purified in acetonitrile. Finally, the PVI@HNTs was vacuum dried at 50 °C.

2.3. Synthesis of the sulfonated poly(aryl ether sulfone)s (SPES)

The SPES was synthesized after borrowing and revising the previous reports [11]. DFDPS (1.271 g, 5 mmol), SDFDPS (2.291 g, 5 mmol), ODP (2.022 g, 10 mmol), TMS (20 mL) and anhydrous K₂CO₃ (2.225 g, 16 mmol) were mixed in a 100 mL flask equipped with a Dean-Stark trap, a magnetic stirrer and a nitrogen inlet. The mixture was stirred for 30 min at room temperature. Then, the mixture was heated with toluene (10 mL) for approximately 4 h at 150 °C to remove the water by toluene. After that the reaction temperature was increased to 180 °C for approximately 12 h, cooled to room temperature later. The resulting polymer was precipitated using absolute ethanol and collected, and washed with hot deionized water to remove inorganic salts. At last, the dried SPES are obtained by vacuum drying at 100 °C for 24 h.

2.4. Preparation of the composite membranes

The SPES was immersed in 2 M sulfuric acid (aq) aqueous solution for 48 h, and dried under vacuum at 100 °C for 24 h to convert -SO₃Na group to -SO₃H group. Disperse a certain amount of PVI@HNTs or HNTs ultrasonically into dimethylformamide (DMF, 5.0 mL) and stir for 8 h. SPES (0.8 g) was mixed with 5 mL of DMF and stirred until a homogeneous solution was formed. Then, the PVI@HNTs dispersion was mixed with the SPES solution, and stirred for 24 h. The solution was casted on the glass and vacuum dried at 70 °C and 100 °C for 12 h, respectively. The composite membrane was designated SPES/HNTs-X or SPES/PVI@HNTs-X, where X is the weight percentage of HNTs or PVI@HNTs relative to SPES.

2.5. Characterization

2.5.1. FTIR and ¹H NMR analysis

FTIR spectrometer (BRUKER VECTOR22) is used to analyze the chemical structure of HNT, PVI @ HNT and composite membrane. The nuclear magnetic resonance instrument (Bruker BioSpin AVANCE 400MHz) using d6-dimethyl sulfoxide (d6-DMSO) as the solvent to collected 1H NMR spectra of SPES membranes.

2.5.2. Thermal stability

All membranes were characterized between room temperature to 800 °C under constant N₂ flow at a heating rate of 10 °C /min by thermogravimetric analysis (TGA, TA-Q600) to analyze its thermal stabilities.

2.5.3. Morphology of the nanotubes and composite membranes

The morphology and microstructure of HNTs, PVI@HNTs and composite membranes were characterized by transmission electron microscopy (TEM, TF20, JOEL 2100F) and scanning electron microscopy (SEM, Nova Nano SEM450). Prior to that, the membranes were fractured in liquid nitrogen and sputtered with gold to expose the cross-section of each membrane.

2.5.4. Mechanical properties

The mechanical properties of the dry composite membranes with the size of 50 mm × 5 mm were evaluated using a microcomputer-controlled universal testing machine (CMT 6104) at a tensile speed of 2 mm/min under room temperature. The average value is calculated by repeating the measurement five times.

2.5.5. Water uptake and swelling properties

First, the membranes (approximately 1 cm × 4 cm) were dried at 100 °C to remove moisture. Then, the dry weight and length of membranes were noted. Samples were soaked in deionized water at different temperatures for 24 h. and wiped the water with soft paper, then weighted and measured lengths to record. Water uptake and swelling values were calculated by the following equation:

$$\text{Water uptake (\%)} = \frac{(W_{\text{wet}} - W_{\text{dry}})}{W_{\text{dry}}} \times 100 \quad (1)$$

$$\text{Swelling ratio (\%)} = \frac{(L_{\text{wet}} - L_{\text{dry}})}{L_{\text{dry}}} \times 100 \quad (2)$$

where W_{wet} and W_{dry} are the weight of the fully hydrated and dry membrane; L_{wet} and L_{dry} are the lengths of the after complete water swelling and dry membrane.

2.5.6. Oxidative stability.

The oxidative stabilities of the composite membranes were evaluated by recording the weights change for 1 h and the dissolution time when the membrane samples disappear of the membrane, with a size of 50 mm × 5 mm which soaking in Fenton's reagent (3% H₂O₂ containing 2 ppm FeSO₄) at 80 °C.

2.5.7. Ion-exchange capacity (IEC) of the membranes

Using the acid-base titration to determine the IEC of the membranes. A membrane sample of a certain weight was cut. The composite membranes were soaked in 1 mol L⁻¹ NaCl solution for 48 h. The solution was back-titrated to neutral with 0.01 mol L⁻¹ NaOH solution by use phenolphthalein as an indicator. The result was calculated by the following equation:

$$\text{IEC} = \frac{(c \times V)}{W_{\text{dry}}} \times 100 \quad (3)$$

where W_{dry} is the weight of the sample (g), V is the volume (L) of NaOH(aq), and c is the concentration (mol L⁻¹) of NaOH solution used in the titration.

2.5.8. Proton conductivity

The proton conductivity of the membranes was tested with electrochemical workstation (CHI660D) by a four-electrode AC impedance method. The tested frequency range with 10 mV AC perturbation, were applied was from 1 Hz to 100 kHz. The membranes were immersed in water for 24 h to hydrated, and measured in deionized water at 20-80 °C. The conductivity was calculated by applying equation:

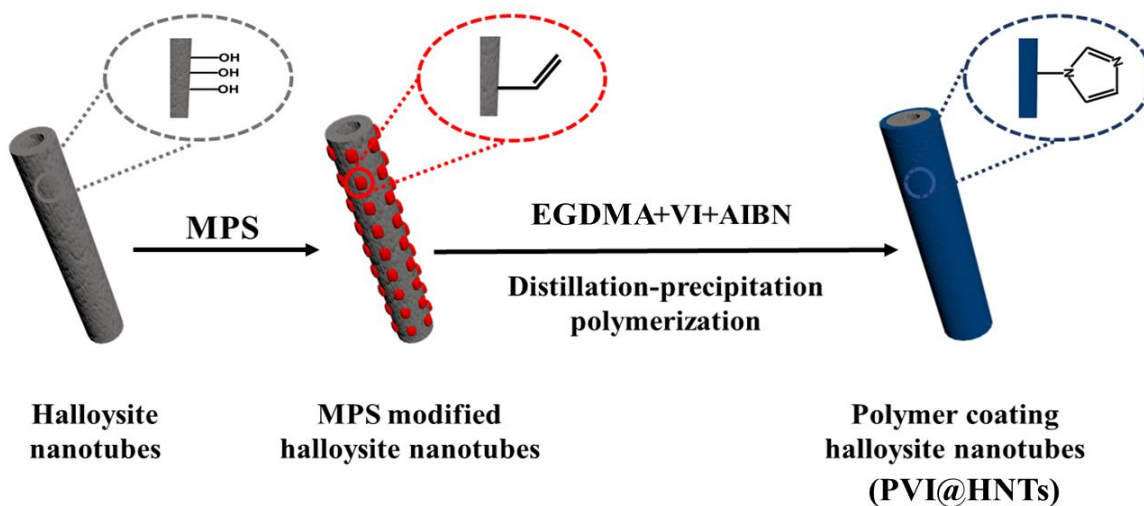
$$\sigma = \frac{l}{(AR)} \quad (4)$$

where σ (S cm⁻¹) represents the proton conductivity of the test membranes, l is the length (cm) of test sample, R (Ω) is the resistance measured of the membranes and A is the effective measurement

area (cm^2) of the membranes.

3. RESULTS AND DISCUSSION

3.1. Preparation of the PVI@HNTs



Scheme 1. Process for the preparation of PVI@HNTs.

The preparation program for the PVI@HNTs is shown in Scheme 1. The PVI@HNTs were prepared by a two-step process. First, the HNTs were modified by MPS to obtain vinyl groups on the HNTs, next a polyvinyl imidazole polymer shells was coated on the surface of the MPS-modified halloysite through distillation-precipitation polymerization. The vinyl of the surface of the halloysite modified by MPS, which facilitated the capture of the newly formed monomers and oligomers, in which EGDMA is a cross-linking agent and VI is a functional monomer.

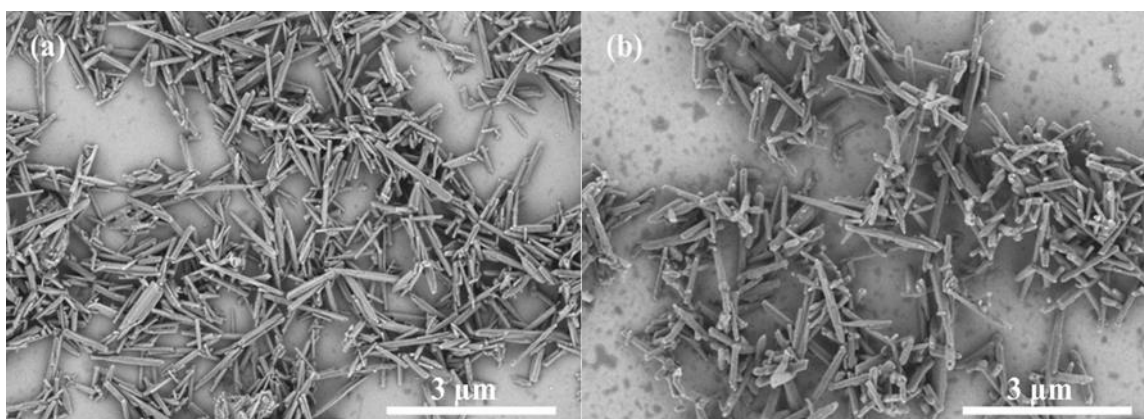


Figure 1. SEM images of (a) HNTs and (b) PVI@HNTs

The microstructures of the HNTs and PVI@HNTs were characterized by SEM (see the

Supplementary Material for results) and TEM, as shown in Fig. 1 and Fig. 2. From Fig. 2(a) and (b) and Fig. 1(a), the HNTs have a distinct tubular structure with lengths between 1 μm and 2 μm and outer diameters between 50 nm and 100 nm. The polymer shell on the outer surface of the HNTs could be clearly seen in Fig. 2(c) and (d) and Fig. 1(b). In addition, PVI@HNTs still have obvious tubular structures. Therefore, the PVI@HNTs exhibit a larger outer diameter than the HNTs, which shows that VI is uniformly polymerized on the surface of the HNTs by precipitation polymerization and that the PVI@HNTs maintain their tubular structure.

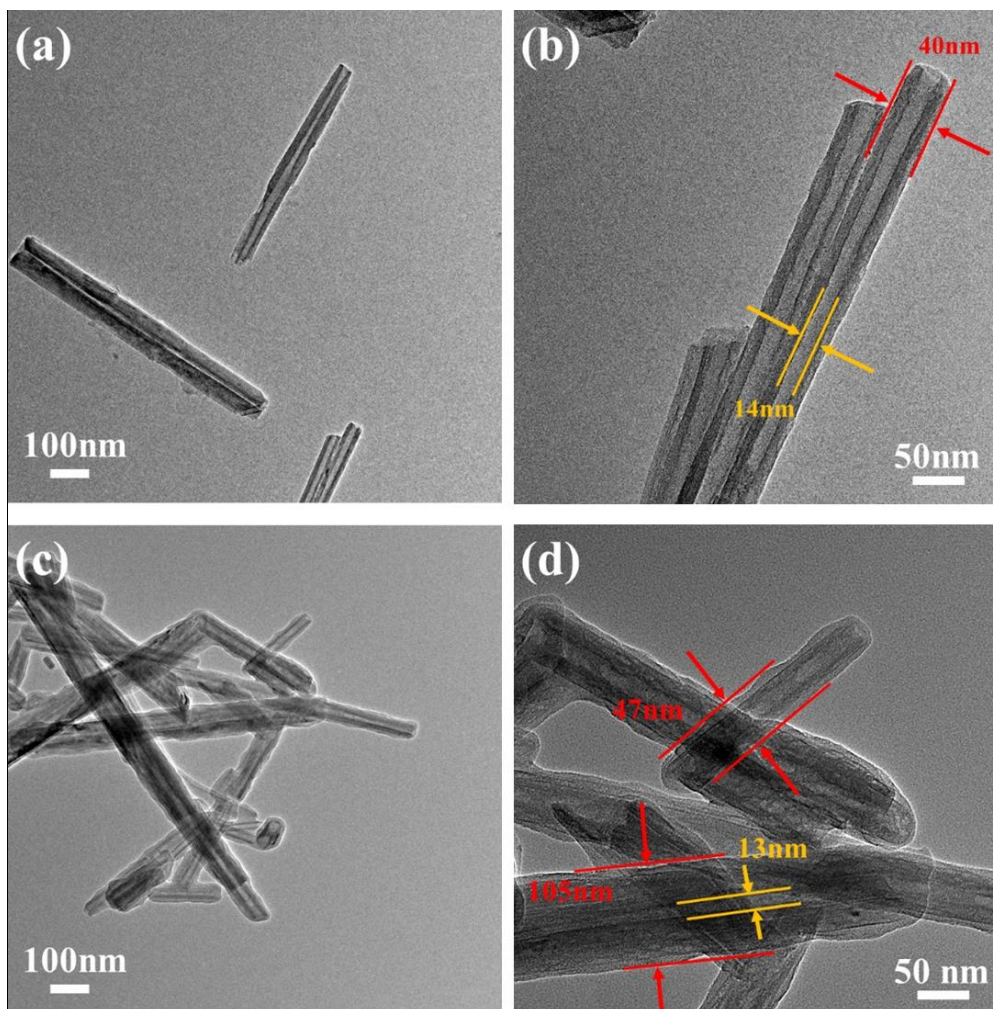


Figure 2. TEM images of (a), (b) HNTs and (c), (d) PVI@HNTs.

FTIR and TGA analyses were determined the appearance and content of the polymer shell on the PVI@HNTs, as shown in Fig. 3. As shown in Fig. 3(a), correspond to the bending and stretching of Si–O–Si, the absorption in the peak at 1034 cm^{-1} and 1096 cm^{-1} appeared for the FTIR spectrum of both HNTs and PVI@HNTs [26]. Due to the –Al–O deformation, a characteristic peak was generated at 915 cm^{-1} [7]. The peaks at 3695 and 3620 cm^{-1} in the spectra of the HNTs and PVI@HNTs were attributed to the stretching vibrations of hydroxyl groups on the cavity of the HNTs [33]. After polymer coating, new peaks appeared at 1640 and 3103 cm^{-1} , which corresponding to the stretching

vibration of the heteroaromatic ring and -N-H of the PVI@HNTs [4.34.35]. A new -CH₂ stretching vibration peak appeared at 2942 cm⁻¹.

Two obvious stages of weightlessness were observed in the TGA curves of both HNTs and PVI@HNTs. The first stage (room temperature to 200 °C) is primarily caused for the steaming of stored water in the nanotubes. The second phase of weightlessness began at 385 °C for the HNTs, while the PVI@HNTs rapidly lost weight starting at approximately 250 °C, and this stage was mainly due to the decomposition of the PVI in the PVI@HNTs. The TGA curves show that PVI@HNTs leave less residue than do the original HNTs, which caused for the decomposition of the PVI in the PVI@HNTs. Based on the TGA results, the PVI content in the PVI@HNTs was calculated as 24.03%. From these results, it can be seen that the polyimidazole was successfully introduced on the surface of HNT.

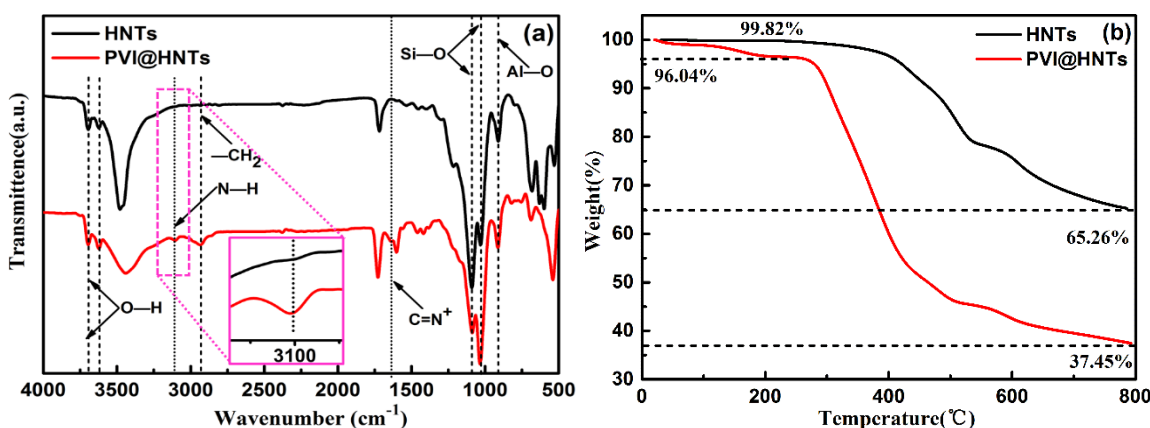
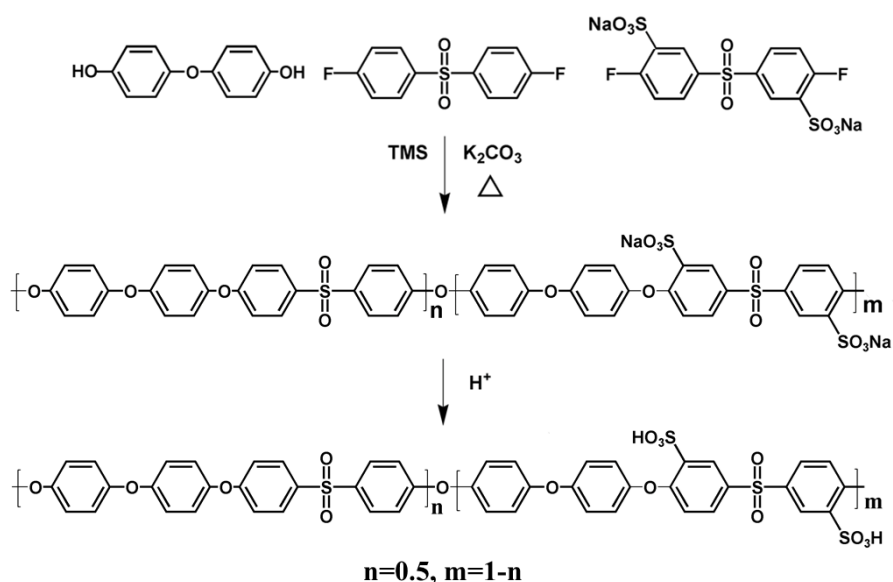


Figure 3. (a) FTIR spectra and (b) TGA curves of the HNTs and PVI@HNTs.

3.2. Synthesis of sulfonated poly(aryl ether sulfone) (SPES) polymer matrix



Scheme 2. Synthesis pathway of SPES.

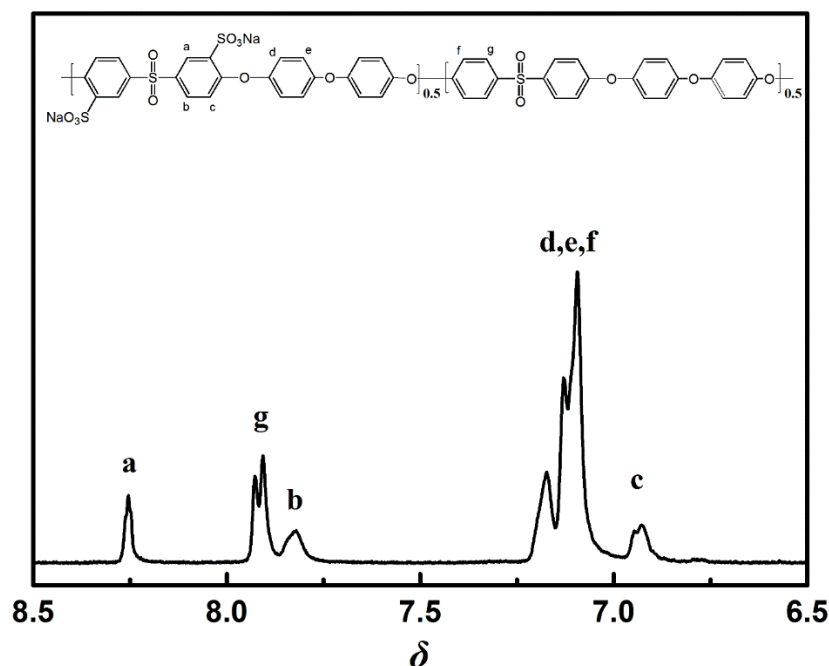


Figure 4. ^1H NMR spectra of SPES

As shown in Scheme 2, through the condensation reaction of DFDPS with SDFDPS and ODP, SPES was successfully prepared. In order for fuel cells to operate efficiently, certain mechanical strength and excellent proton conductivity are essential for PEM. Therefore, in this study, By controlling the ratio of difluoromonomers (DFDPS and SDFDPS) participating in the reaction to 1: 1, SPES with a sulfonation degree (DS) of 50 mol% can be intentionally synthesized [9]. The chemical structure of SPES was analyzed through ^1H NMR spectroscopy, which presented in Fig. 4. The proton distribution data given in the figure is consistent with its molecular structure. Since the feed monomer ratio of DFDPS to SDFDPS is 1:1, a DS of 50 mol% was expected. The degree of sulfonation of SPES-50 derived from the ^1H NMR results according to the previously reported calculation method is consistent with the expected results [36]. As indicated by ^1H NMR spectroscopy, the protons in the nonsulfonated monomer appear at 7.82 ppm and the protons adjacent to the sulfonic acid appear at 8.25 ppm, and the polymer structure could be analyzed according to the ratio of the two peak areas. The sulfonation degree can be calculated by Eq(5):

$$\text{Sulfonation degree(\%)} = \frac{a/2}{\left(\frac{a}{2} + \frac{g}{4}\right)} \times 100 \quad (5)$$

where a and g refer to the integrated areas of the two protons peaks, separately. The calculated sulfonation degree was 46%, which is close to what was expected based on the monomer feed ratio, indicating that the polymerization has occurred successfully. The deviation may be due to the slight difference in reactivity between DFDPS and SDFDPS caused by the differences in their chemical structures, as reported by others [10.37].

3.3. Preparation of the composite membranes

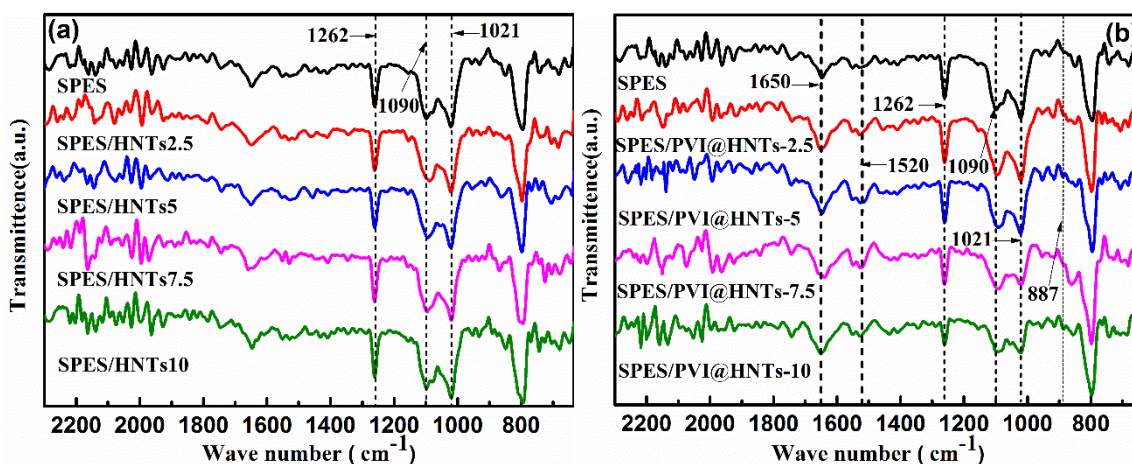


Figure 5. FTIR spectra of the SPES and composite membranes

The composite proton exchange membranes were prepared by incorporating HNTs or PVI@HNTs into the SPES matrix. By analyzing the infrared spectrum of the composite film, study the interaction between the polymer matrix and fillers and the chemical structure of the composite membranes. As shown in Fig. 5, the tensile vibration absorption peaks of O=S=O in the $-\text{SO}_3\text{H}$ group appear in the spectra of all the membranes, at 1262, 1090, and 1021 cm^{-1} respectively [7,38]. Compared with that of the SPES control membrane, there are no obvious new peaks in the spectrum of the composite membrane, which may be caused for the shielding of the groups responsible for the peaks in spectrum of the SPES membrane. As shown in Fig. 5(a), the spectra of the SPES/HNTs-*X* composite membranes do not show any new peaks or significant changes compared to those of the SPES membrane, revealing that the added HNTs and the SPES matrix are only physically mixed and do not form chemical bonds [7]. As illustrated in Fig. 5(b), the peak intensities for the O=S=O absorption bands of the SPES/PVI@HNTs-*X* membranes are weaker compared with that of the SPES membrane, showing the generation of $-\text{S}=\text{O}\cdots\text{H}-\text{N}=\text{}$ bonds at the SPES and PVI@HNTs interface [3]. A peak at approximately 887 cm^{-1} , indicated that the protons in the $-\text{SO}_3\text{H}$ group have dissociated and formed $-\text{S}-\text{O}-$ groups [39]. Furthermore, compared with SPES control membrane, the absorption peaks at 1650 and 1520 cm^{-1} in the spectra of the SPES/PVI@HNTs-*X* composite membranes are more intense, which may be caused for the structure of $^+\text{H}-\text{N}=\text{}$ and $^+\text{H}-\text{HN}-$ groups [40]. The nitrogen atoms of the imidazole group would be protonated, resulting in attractive interactions between the PVI@HNTs and SPES in the form of $-\text{S}-\text{O}^-\cdots^+\text{H}-\text{HN}-$ and $-\text{S}-\text{O}^-\cdots^+\text{H}-\text{N}=\text{}$ [4,39].

3.4. Microscopic morphology and EDX of the SPES and composite membranes

A photograph of SPES/ PVI@HNTs-7.5 is shown in Fig. 6(a). From Fig. 6(a), we can see that the membrane is transparent and flat.

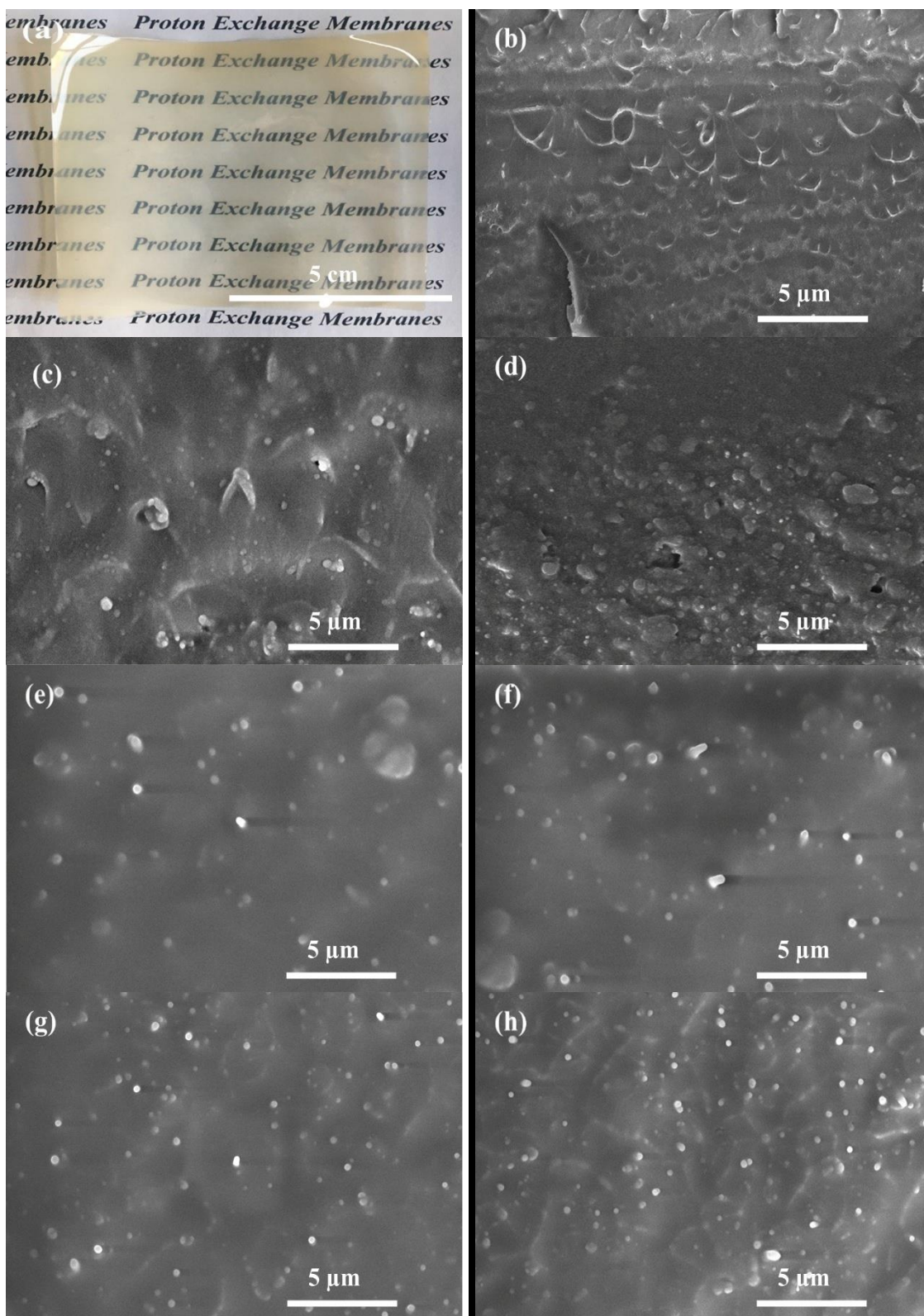


Figure 6. (a) Photograph of SPES/PVI@HNTs-7.5 and SEM images of the cross sections of the membranes: (b) SPES, (c) SPES/HNTs-2.5, (d) SPES/HNTs-7.5, (e) SPES/PVI@HNTs-2.5, (f) SPES/PVI@HNTs-5, (g) SPES/PVI@HNTs-7.5 and (h) SPES/PVI@HNTs-10.

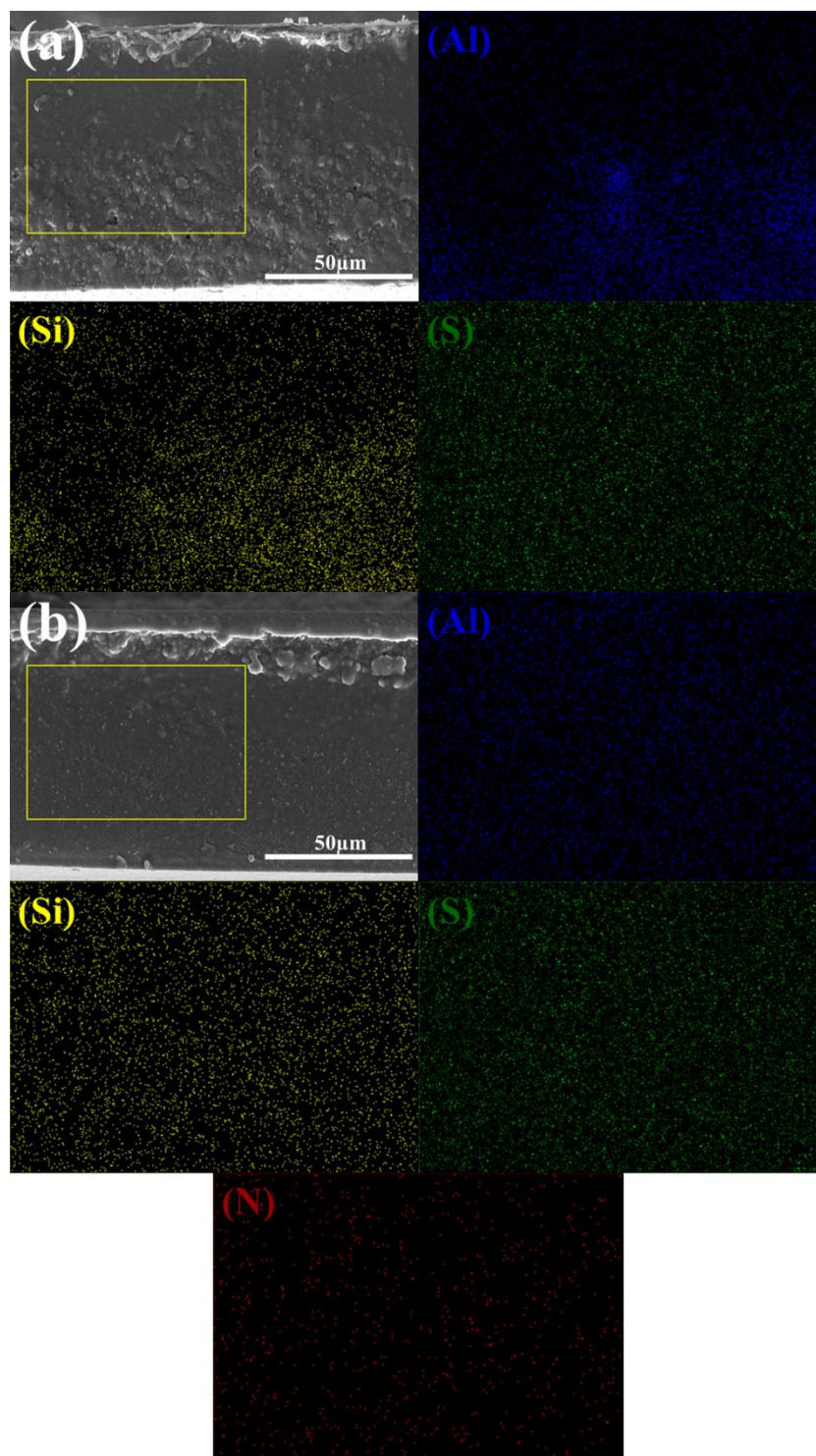


Figure 7. (a) Cross-sectional SEM images and aluminum element, silicon element, sulfur element EDX mapping images of SPES/HNTs-7.5; (b) Cross-sectional SEM images and aluminum element, silicon element, sulfur element and nitrogen element EDX mapping images of SPES/PVI@HNTs-7.5.

The dispersity of the fillers and the cross-sectional morphology of the membranes could be seen in Fig. 6(b) - Fig. 6(f). The cross sections of the SPES membrane are flat and dense and lack significant voids (Fig. 6(b)). However, Due to the poor compatibility of HNT surface with SPES, the

cross-section micrographs of the SPES/HNTs-X membranes show more voids (Fig. 6(c) and (d)).

The white substances can be observed in the cross-section SEM images of the SPES/PVI@HNTs-X membranes. More spots and rod-like substances appeared in the matrix (Fig. 6(e) - Fig. 6(h)), with the loading of the PVI@HNTs increased. These spots and rod-like substances represent the PVI@HNTs in the SPES/PVI@HNTs-X membranes. The PVI@HNTs is well dispersed in the SPES, except for the trace amounts of agglomerates in SPES/PVI@HNTs-10, almost no agglomeration was observed in the composite membranes. After careful examination of the images of the PVI@HNTs, the interface between the PVI@HNTs and SPES is murky, which indicates that the PVI@HNTs have well interfacial binding to the SPES matrix. The good dispersion of the PVI@HNTs may generate a much number of surface-induced pathways to create continuous pathways for proton transport within the SPES.

The dispersions of the nanofiller in the membranes were investigated by EDX analysis. The bright dots of different colors in the figure represent different elements. EDX elemental mapping of the cross-section of SPES/HNTs-7.5 was performed, and the maps of aluminum, silicon and sulfur are shown in Fig. 7(a). As shown in Fig. 7(a), the HNTs are unevenly distributed in the cross-section of SPES/HNTs-7.5. The corresponding elemental maps of aluminum and silicon confirms this poor distribution. The elemental mapping showed that sulfur is dispersed homogeneously throughout the entire cross-section. Fig. 7(b) shows the SEM image of the cross-section of the SPES/PVI@HNTs-7.5 composite membrane and the corresponding EDX mapping. The maps of Si, Al, and N indicated they were uniformly distributed throughout the PVI@HNTs-7.5 membrane because of the interactions between the PVI@HNTs and the SPES. Furthermore, the elemental map of sulfur shows that the -SO₃H groups in the polymer are uniformly dispersed throughout the cross-section of the SPES/PVI@HNTs-7.5 composite membrane.

3.5. Thermal and mechanical properties of the composite membranes

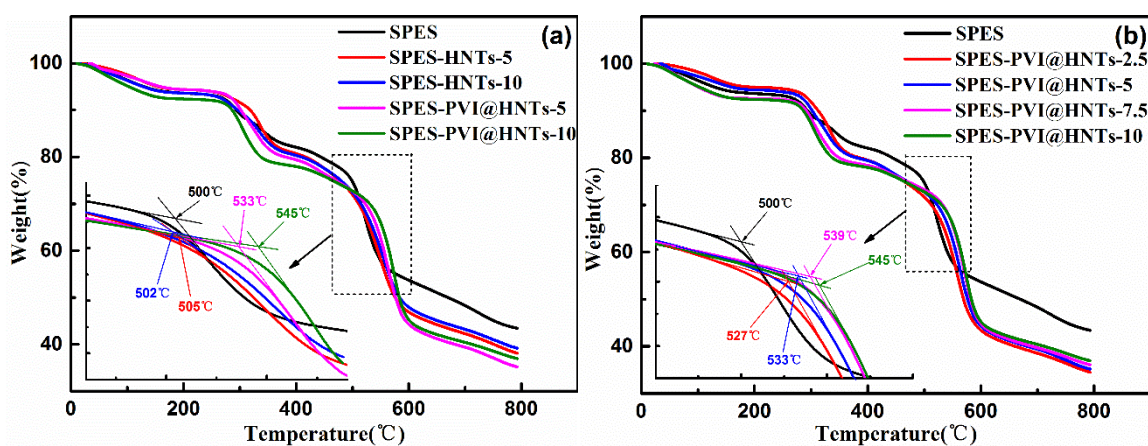


Figure 8. TGA curves of the SPES and SPES/PVI@HNTs-X

The thermal stability of the PEM is an essential requirement for the operational life of a fuel cell. The thermal stability of each membrane was studied by TGA under a N₂ flow. As shown in Fig. 8. Each membrane sample showed three obvious stages of weightlessness. Due to the steaming of bond

and free water on the membranes, the weightless that occurred below approximately 200 °C. The weightless between 250 °C and 380 °C was mostly associated with the degradation of the polymer shell of PVI@HNTs and the $-SO_3H$ groups, and the weightless that occurred between 480 °C and 800 °C was mostly caused for the degradation of the SPES. As shown in Fig. 8(a), the decomposition temperature of the SPES/HNTs-*X* in the third stage was not significantly different than that of the SPES, while the initial decomposition temperature of the third stage of SPES/PVI@HNTs-*X* degradation was higher. As shown in Fig. 8(b), as PVI@HNTs loading raise, the initial decomposition temperature of the polymer backbone increased from 500 °C of SPES to 544 °C for SPES/PVI@HNTs-10. There may be strong interactions between the surface of the PVI@HNTs and the SPES interface, which would hinder the decomposition of the polymer backbone. This finding is consistent with the results of other related studies [41.42]. In addition, the residual carbon ratio of the SPES and the SPES/HNTs-*X* was higher than that of the SPES/PVI@HNTs-*X* after the test, which may be caused by the degradation of the polymer shell on the PVI@HNTs. Similar phenomena have been found in other studies [7.43.44]. Collectively, as the TGA results shown that, the thermal stabilities of all membranes meet operating temperature of fuel cells.

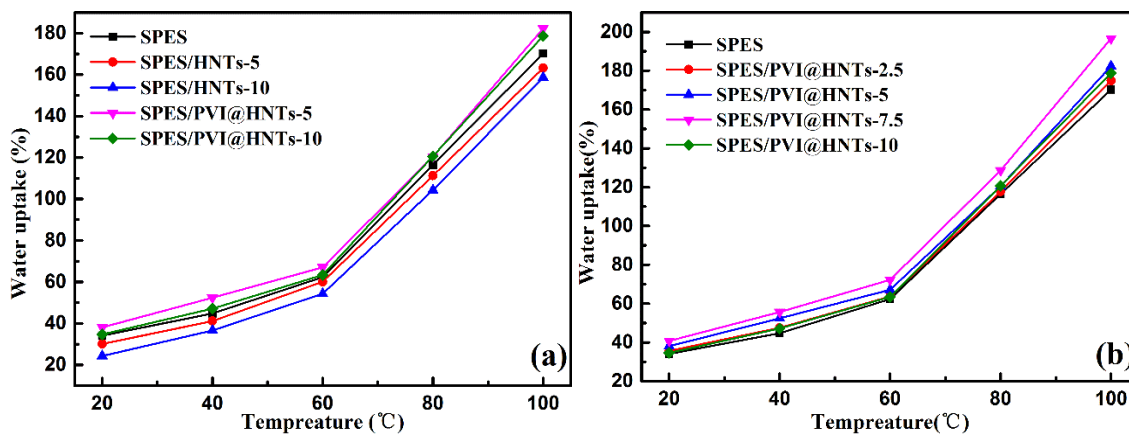
In addition, the mechanical properties of proton exchange membranes are necessary for fuel cell. Table 1 summarizes the mechanical properties of all membranes. The SPES membrane has an outstanding mechanical stability with elongation at break of approximately 104.2% and a tensile strength of 45.9 MPa. The tensile strengths of the SPES were higher than the SPES/HNTs-*X*, except for the tensile strength of the SPES/HNTs-5, which was slightly higher than that of the SPES. Furthermore, the elongation at break of the SPES/HNTs-10 is only 19%., which were substantially lower than that of the SPES. These results are mainly due to the reinforcing effect of the inorganic filler, which increases the tensile strength of the SPES/HNTs-5 composite membrane. However, HNTs aggregation results in the generation of defects and voids within the membrane, which could decrease the mechanical properties of the membranes [7]. Under identical conditions, compared with that of the SPES and the SPES/HNTs-*X*, incorporating PVI@HNTs notably increases the mechanical stabilities of membranes. With the PVI@HNTs content was increased from 2.5% to 7.5%, the tensile strength increased from 47.9 to 57.4 MPa; the tensile strength of the SPES/PVI@HNTs-7.5 membrane reached a maximum of 57.4 MPa, which is an increase of 25.1% compared to that of SPES. The enhancement in the mechanical properties of SPES/PVI@HNTs-*X* can be caused for the formation of acid-base pairs ($-S-O^- \cdots ^+H-N=$ and $-S-O^- \cdots ^+H-HN-$) between the PVI@HNTs and SPES. The strong electrostatic attractive force at the PVI@HNTs \cdots SPES interface can greatly restrain the chain mobility of SPES and facilitate the stress turn over from the polymer matrix to the PVI@HNTs [45.46]. The tensile strength of the membrane reaches 54.2 MPa with the PVI@HNTs content increased to 10%, which can be attributed to PVI@HNTs aggregation and the stress concentration produced in the membrane [47]. Similar to the SPES/HNTs-*X* composite membrane, the elongation at break of the SPES/PVI@HNTs-*X* composite membrane also decreases due to increasing filler content. However, the electrostatic interaction between the interfaces increasing the plasticity of the SPES, the SPES/PVI@HNTs-*X* composite membranes maintain a high elongation at break, and the elongation at break of SPES/PVI@HNTs-10 can still reach 52.9% [26]. In summary, compared with SPES, SPES/PVI@HNTs-*X* possesses higher mechanical stability.

Table 1. Water uptake, swelling ratio and mechanical properties of the membranes

Sample	Water uptake (%)		Swelling ratio (%)		Tensile strength (MPa)	Elongation at break (%)
	20 °C	80 °C	20 °C	80 °C		
SPES	34.1	116.5	16.4	44.5	45.9	104.2
SPES/HNTs-2.5	32.4	118.9	16.3	43.1	45.4	43.1
SPES/HNTs-5	30.1	111.3	15.9	42.6	46.2	35.3
SPES/HNTs-7.5	26.7	107.5	15.3	37.9	43.5	25.7
SPES/HNTs-10	24.3	104.4	14.4	36.2	42.9	16.9
SPES/PVI@HNTs-2.5	35.7	117.7	12.2	38.3	47.9	90.4
SPES/PVI@HNTs-5	38.1	120.5	12.9	40.4	50.6	62.7
SPES/PVI@HNTs-7.5	40.8	128.6	14.2	45.9	57.4	63.5
SPES/PVI@HNTs-10	34.7	120.7	11.8	35.4	54.2	52.9

3.6. Water uptake and swelling ratio of the membranes

Water absorption is a significant property of PEM, due to water molecules are indispensable for proton transport. The water uptake values and swelling ratios of SPES, SPES/HNTs-X and SPES/PVI@HNTs-X at 20 °C and 80 °C are recorded in Table 1, respectively. The water uptake values and swelling ratios of the different membranes at temperatures ranging from 20-100 °C are shown in Fig. 9. As shown in Fig. 9(a) and (b), the water uptake and swelling degrees of all membranes increased with temperature due to increased the water diffusivity and elevated chain mobility. As displayed in Fig. 9(a) and Table 1, the water uptake values of the SPES reached 34.1% and 116.5% at 20 °C and 80 °C, respectively.



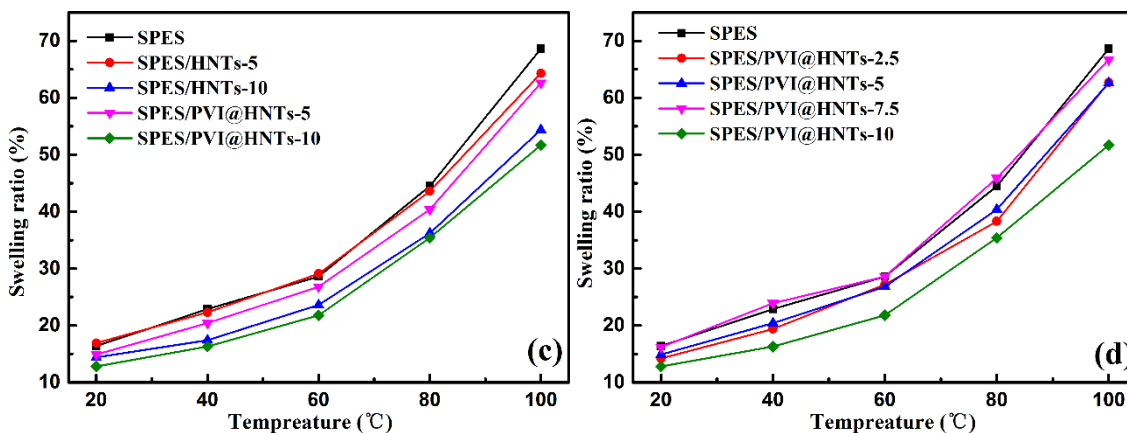


Figure 9. (a and b) Water uptake of the SPES and composite membranes; (c and d) swelling ratio of the SPES and composite membranes.

However, owing to the uneven dispersion of HNTs in SPES, the water adsorption capacity of SPES/HNTs- X was weaker than the SPES matrix [7]. The water uptake values of SPES/PVI@HNTs- X increase to a certain extent with increasing PVI@HNTs loading, and the water absorption of the SPES/PVI@HNTs-7.5 was the highest. This result could be attributed to the nitrogen atoms of shell of polyvinyl imidazole easily binds water molecules to form a hydrogen bonding network [31]. In addition, this is similar to plant cells storing water through a capillary storage mechanism, storing water in the lumen of PVI@HNTs [48]. Therefore, the water absorption capacities of the SPES/PVI@HNTs- X composite membranes were improved relative to the SPES and SPES/HNTs- X membranes, as shown in Table 1 and Fig. 9(b). However, further increasing the filler content caused the water absorption rate of SPES/PVI@HNTs- X to begin to decrease. For instance, at 80 °C, adding the PVI@HNTs content from 2.5% to 7.5% increased the water uptake capacity of the SPES/PVI@HNTs- X membrane monotonically from 117.7% to 128.6%. When the PVI@HNTs content was further increased, the water uptake decreases to 120.7% for SPES/PVI@HNTs-10. This behavior may be related to the strong electrostatic attractive force at the PVI@HNTs...SPES interface. The water absorption space in the SPES matrix is restricted, due to the narrowing of the ion transmission channel, which is caused by strong electrostatic attraction [7].

The swelling ratio is an excellent factor affecting the dimensional stability of the PEM. Generally, water adsorption in the polymer matrix may cause swelling of a membrane [49]. The lower swelling ratio of the SPES/HNTs- X composite membrane than the SPES membrane is mainly caused for the reduced water uptake of the SPES/HNTs- X and the chain mobility of SPES [26], as shown in Table 1 and Fig. 9(c). As indicated in Fig. 9(d) and Table 1, with the increasing of the content of the PVI@HNTs, swelling ratios of the SPES/PVI@HNTs- X membranes increased, and the ratio increased from 38.3% for SPES/PVI@HNTs-2.5 to 45.9% for SPES/PVI@HNTs-7.5 at 80 °C. When the content of PVI@HNTs was increased to 10%, the swelling ratio of SPES/PVI@HNTs-10 decreased to 35.4%. The swelling ratios of SPES/PVI@HNTs- X are still lower than those of SPES/HNTs- X and SPES. Such performance may be caused for three factors. (i) The added water absorption results in more water molecules in hydrophilic clusters, increasing the swelling ratio. The swelling ratios of the SPES/PVI@HNTs- X membranes are related to their water absorption, and the swelling ratios change

with water absorption [49]. (ii) PVI @ HNT can store some water inside due to capillary action, which increases the moisture absorption but does not lead to the polymer matrix swelling. (iii) The swelling space of SPES is restricted caused for the narrowing of ion transmission channel due to strong electrostatic attraction [3.7.40]. In conclusion, compared to SPES/HNTs-*X* and SPES, the SPES/PVI@HNTs-*X* possesses higher dimensional stability, and may be adequate for applications of fuel cell.

3.7. Oxidative stability of the membranes

Because the proton exchange membrane is inevitably in contact with air during use and in the fuel cell operating environment, the anode will generate free radicals such as HOO• and HO•, which will rapidly lead to decomposition of the membrane [50]. Thence, the oxidative stability of a proton exchange membrane has an important affect on the normal use of a PEMFC. The oxidative stability of each membrane was determined at 80 °C through the time required for the sample to dissolve in Fenton's reagent, and weightless after treatment with Fenton's reagent for 60 min. The data are recorded in Table 2.

Table 2. Proton conductivity, IEC and oxidative stability data of the different membranes

Sample	Proton Conductivity (S cm ⁻¹)		IEC (mequiv. g ⁻¹) experimental	Oxidative stability	
	40 °C	80 °C		RW (%) ^a	τ (min) ^b
SPES	0.059	0.136	1.72	92.4	>120
SPES/HNTs-2.5	0.057	0.127	1.69	92.8	>150
SPES/HNTs-5	0.043	0.114	1.65	93.4	>150
SPES/HNTs-7.5	0.041	0.109	1.63	93.9	>150
SPES/HNTs-10	0.031	0.091	1.59	94.4	>150
SPES/PVI@HNTs-2.5	0.077	0.141	1.65	96.5	>180
SPES/PVI@HNTs-5	0.087	0.169	1.62	96.8	>180
SPES/PVI@HNTs-7.5	0.095	0.198	1.58	97.2	>180
SPES/PVI@HNTs-10	0.096	0.176	1.56	98.1	>180

^a The remaining mass of the membranes after treatment with Fenton's reagent for 1 h.

^b Membrane dissolution time in Fenton's reagent at 80 °C

The oxidative stabilities of both SPES/HNTs-*X* and SPES/PVI@HNTs-*X* composite membranes increased with increasing filler content, and their stabilities were all greater than that of the

SPES membranes. Notably, the SPES/PVI@HNTs-X composite membranes exhibited the best oxidative stability, and they were significantly more stable than the SPES membrane. This phenomenon could be attributed to the composite membranes having lower swelling volumes and lower IEC values, which reduce the chance for oxidative radicals to damage the polymer structure. Furthermore, due to the strong electrostatic attraction between the PVI @ HNTs and SPES interface, peroxide is prevented from penetrating into the membrane [51]. The above results indicated that SPES/PVI@HNTs-X composite membranes had acceptable oxidative stabilities.

3.8. IEC, proton conductivity and proton transfer mechanism

The IEC is a significant measure of the ion-exchange performance of a proton exchange membrane.

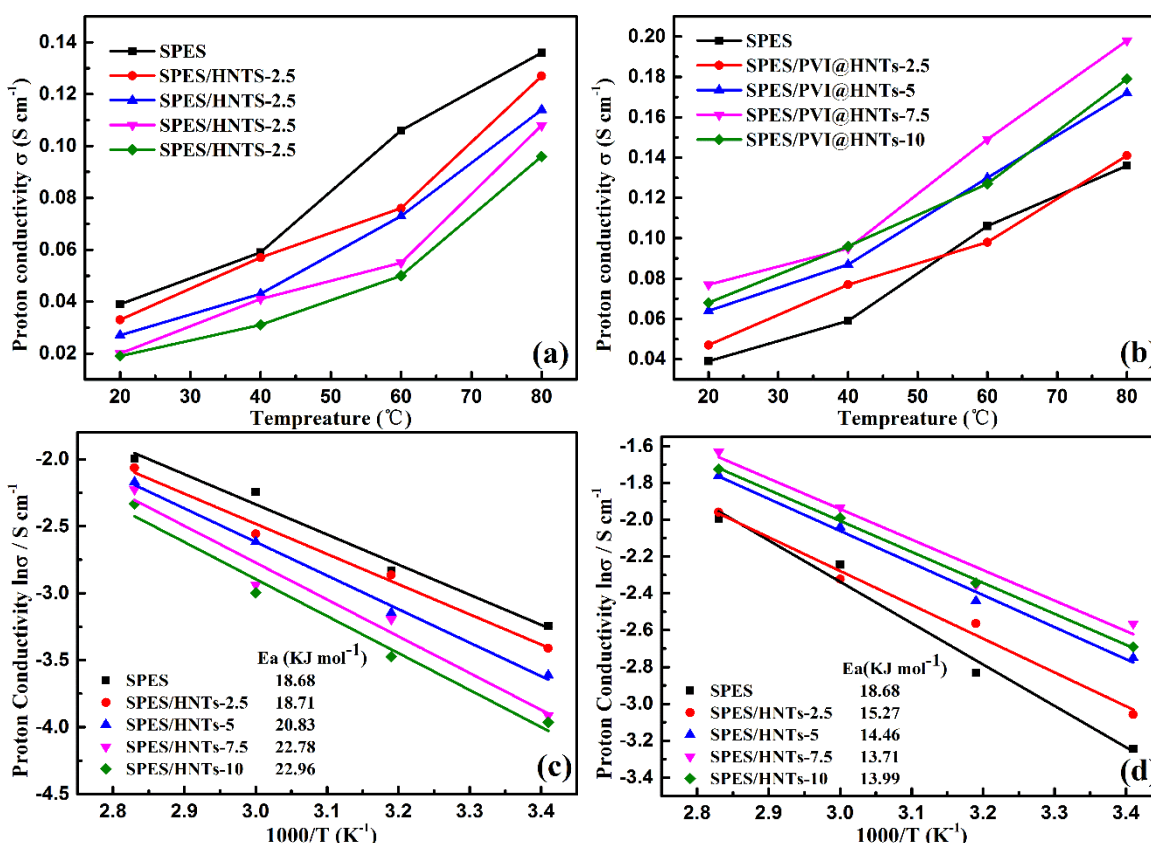


Figure 10. (a and b) Proton conductivity of the SPES membrane and composite membranes under fully hydrated conditions as a function of temperature; (c and d) Arrhenius plots of conductivity as a function of temperature for the SPES membrane and composite membranes.

The theoretical IEC value of the SPES was calculated to be 1.87 mequiv. g⁻¹ [32,36]; as shown in Table 2, the experimental IEC of the SPES membrane consistent with previous data, is 1.72 mequiv. g⁻¹, and these data are in well agreement. As the increasing of filler content, the IEC values of the composite membranes gradually decrease. The addition of HNTs decreases the sulfonic acid groups

density, which reduces the IEC value of the SPES/HNTs-*X* membranes, may be caused for the low dissociation degree of $-(\text{Al/Si})-\text{OH}$ [3]. The IEC values of SPES/PVI@HNTs-*X* are lower than that of the SPES/HNTs-*X*. The IEC values of SPES/PVI@HNTs-*X* varied from 1.65 to 1.56 mequiv g^{-1} . For the SPES/PVI@HNTs-*X* composite membranes, the H^+ dissociation from the acidic groups were restricted through the acid-base interactions between the sulfonic acid groups and the heterocycles, so as the content of PVI@HNTs increases, the number of exchangeable protons per unit mass decreases [40].

Proton conductivity influences the operational output of the fuel cell, is the basic Influence factor of PEM [39]. Fig. 10 depicts the proton conductivity of all membranes at different temperatures when fully hydrated. Table 2 lists the proton conductivity data of all membranes at 40 °C and 80 °C when fully hydrated. Table 2 shows that the SPES exhibits a proton conductivity of 0.136 S cm^{-1} when was fully hydrated at 80 °C. In contrast, HNTs incorporation decreases the proton conductivity of SPES/HNTs, which is in agreement with reported result [7.26]. Meanwhile, the proton conductivity elevated from 0.127 to 0.067 S cm^{-1} as the HNTs content elevated from 2.5% to 10%, as shown in Table 2. As illustrated in Fig. 10(a), the proton conductivity of SPES/HNTs-*X* composite membranes decreases with increasing HNTs content and lower than that of SPES between 20 °C and 80 °C. The reduced proton conductivity may be caused for the following factors: (i) the incorporation of HNTs will reduce hydrogen networks and proton carriers, is caused for decreases the water uptake, and (ii) decrease of IEC value, which will reduce the sites of proton transfer; (iii) the poor dispersion of the HNTs in the SPES matrix destroys the proton transmission network, which will increase the transfer resistance of hydronium ions and protons [26.52.53]. Fig. 10(b) illustrates the proton conductivity of SPES/PVI@HNTs-*X* and SPES under fully hydrated conditions at different temperatures. The SPES membrane and the SPES/HNTs-*X* composite membranes show dramatically worse proton conductivity than is seen with the SPES/PVI@HNTs-*X* composite membranes. PVI@HNTs incorporation increases the proton conductivity of SPES/PVI@HNTs-*X* when the PVI@HNTs content is below 7.5%, but when the PVI@HNTs content is higher than 7.5%, the proton conductivity of this membrane is reduced. As illustrated in Table 2, the proton conductivity of the SPES/PVI@HNTs-7.5 composite membrane attained 0.198 S cm^{-1} at 80 °C when was fully hydrated, which was 46% higher than SPES and higher than most previously reported works on modified PEMs, as shown in Table 3.

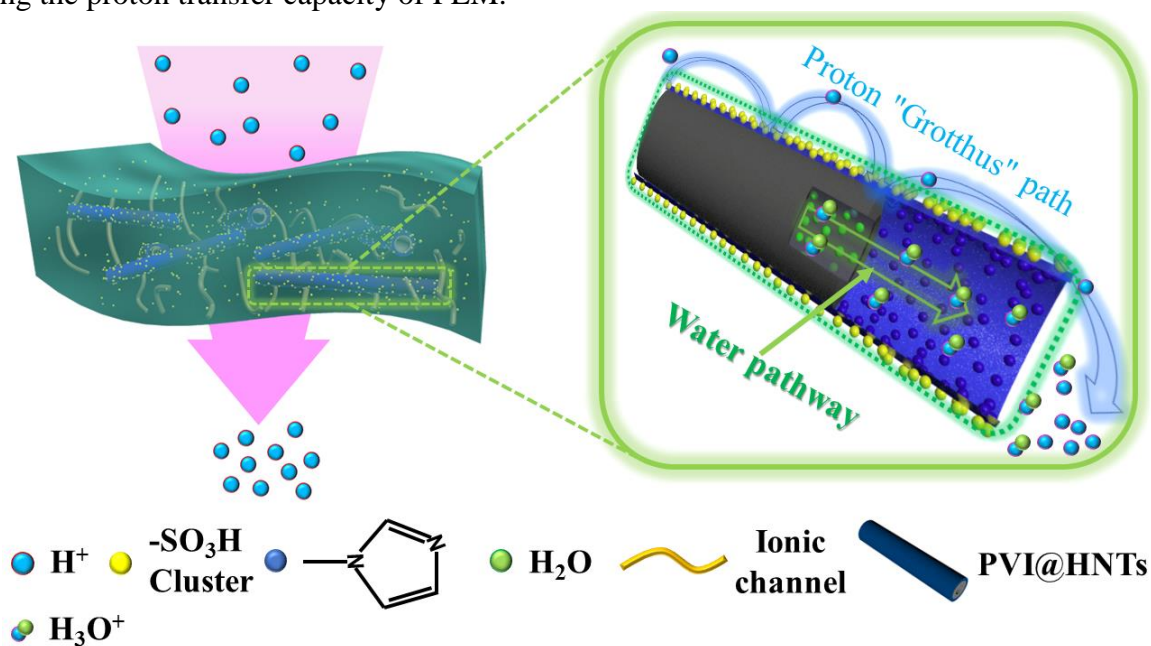
Table 3. Comparisons of proton conductivity.

Membranes	Testing condition	Proton conductivities (S cm^{-1})	References
SFPEKK-60/NCC-4	90 °C, fully hydrated conditions	0.245	[54]
SPES/Cell-5	80 °C	0.13	[55]
SFG-PPEK-4	80 °C, 100% RH	0.184	[56]

SPAE-TM20	80 °C, 100% RH	0.256	[57]
SPAEKS-80/PWA-IL	80 °C, fully hydrated conditions	0.127	[58]
SFPEEKK5/sNCC-5	80 °C, fully hydrated conditions	0.242	[59]
PAES-sPOSS-14	80 °C, fully hydrated conditions	0.142	[60]
Sulfonated GO/Nafion	100 °C	0.12	[61]
SFPAEK/NCC-4	80 °C, fully hydrated conditions	0.187	[62]
SP/Cr-fa-SPA-40	80 °C	0.11	[63]
1F-SPAES-40	80 °C	0.120	[64]
SPAEK/PW-mGO 1 wt%	80 °C, 100% RH	0.26	[65]
SPT-4	120°C	0.166	[66]
Ph-SPEEKK-sNCC-4	80 °C, fully hydrated conditions	0.115	[67]
Nafion/SCNT-5%	80 °C, 100% RH	0.193	[68]
SPES/PVI@HNTs-7.5	80 °C, fully hydrated conditions	0.198	This work

The excellent proton transfer ability of the SPES/PVI@HNTs-*X* composite membranes can be explained by the proton transfer mechanism, which is illustrated in Scheme 3. On the whole, there are two proton transfer mechanisms in PEMs: the “Grotthuss mechanism” and the “Vehicle mechanism” [69]. Under the Grotthuss mechanism, proton transfer mostly depends on the hydrogen bonding network between adjacent ion clusters and the acid-base groups. Protonated water molecules (H_3O^+ , H_5O_2^+) can diffuse protons to the hydrophilic region under the vehicle mechanism. The obviously enhance of proton conduction performance could be explained as follows: (i) The proton donors and proton acceptors are contacted through the acid-base pairs which consists of imidazole groups and sulfonic acid at the PVI@HNTs...SPES interface, promoting the protonation/deprotonation of those. These acid-base pairs with a low energy barrier, create continuous pathways for ultrafast proton transfer via the Grotthuss mechanism [4.70]. (ii) By the acid-base pairs ($-\text{S}-\text{O}-\cdots+\text{H}-\text{HN}-$ and $-\text{S}-\text{O}-\cdots+\text{H}-\text{N}=\text{}$), extensive, one-dimensional, continuous, long-range proton nanochannels are formed on the PVI@HNTs these channels are convenient route for ultrafast proton transfer [28]. (iii) The PVI@HNTs connect the independent proton transfer channels as bridges to construct a fast proton transmission network [11]. (iv) The hollow cavities of the PVI@HNTs contain a large amount of -OH groups, allowing the cavities to serve as water storage centers and hydrated fast proton transfer channels. Thus, the vehicle-type proton transfer mechanism is enhanced. The interactive improvement

of the “Grotthuss mechanism” and the “Vehicle mechanism” ensures high proton transfer in SPES/PVI@HNTs-X. However, the agglomeration of extra PVI@HNTs may block the channels and decrease the proton conductivity. Analogous phenomenon has been recorded in other papers [3.19.51.62]. Regarding the effect of nanofillers on the proton conduction of composite membranes, the activation energy of SPES and composite membranes is estimated by Arrhenius equation, as shown in Fig. 10(c) and 10(d). The activation energies of SPES/HNTs-X were in the range of 18.71-22.96 kJ mol⁻¹, which are higher than that of SPES, since SPES has a high proton transfer energy barrier of 18.68 kJ mol⁻¹. The higher energy barrier is mostly caused for the poor dispersion of the HNTs in the SPES, which destroys the transmission network of proton, increasing the proton transfer energy barrier. The higher activation energy indicates that proton transfer is more difficult [3]. Compared with the high energy barrier in the SPES and SPES/HNTs-X membranes, the SPES/PVI@HNTs-X composite membranes show lower proton transfer barriers, and the E_a values for SPES/PVI@HNTs-2.5, SPES/PVI@HNTs-5, SPES/PVI@HNTs-7.5 and SPES/PVI@HNTs-10 are 15.27, 14.46, 13.71, and 13.99 kJ mol⁻¹, respectively. The smaller activation energies indicated easier proton transfer, suggesting that proton with a low energy barrier can ultrafast transmit by continuous pathways, which created by the interaction of the imidazole - sulfonic acid groups on the PVI@HNTs...SPES interface [35]. However, since the agglomeration of PVI@HNTs disrupts the proton transfer network, SPES/PVI@HNTs-10 shows a proton transfer activation energy that is higher than that of SPES/PVI@HNTs-7.5. These proton transfer activation energies of the membranes are consistent with the results of proton conductivity. These findings imply that the construction of a continuous long-range one-dimensional proton transfer pathway by the acid-base interactions performs a major effect in improving the proton transfer capacity of PEM.



Scheme 3. The suggested proton transfer mechanism in the SPES/PVI@HNTs-X.

4. CONCLUSIONS

Inspired by biological systems, a simple method of constructing a highly efficient proton transfer channels in a polymer matrix was developed by incorporating polyvinylimidazole/halloysite core-shell nanotubes (PVI@HNTs) into an SPES matrix. PVI@HNTs was successfully synthesized through distillation-precipitation polymerization. The internal cavities of the PVI@HNTs were rich in -OH, forming fast water-transport channels (similar to those in the transport tissue of plants); the shell of the polyvinylimidazole layer formed an acid-base pair (similar to those in cell membrane proton pumps) which can build a proton transfer path and provide a one-dimensional fast channel for protons. Through the joint action of the “Grotthuss mechanism” and the “vehicle mechanism”, the proton transfer performance of SPES/PVI@HNTs-*X* composite membranes can be enhanced. In addition, the high aspect ratio PVI@HNTs connected the proton transfer channels to each other, especially the dead ends, improving the efficacy of proton transport channels. The proton conductivity of SPES/PVI@HNTs-7.5 obtained 0.198 S cm^{-1} when fully hydrated at $80 \text{ }^\circ\text{C}$, which was 46% higher than SPES. In addition, the water uptake, anti-swelling performance, antioxidant performance and mechanical strength of the membranes have been improved duo to the introduction of the PVI@HNTs. Through systematic research, the SPES/PVI@HNTs-*X* composite membranes were demonstrated to have good overall performance, and they show good application prospects in PEMFC.

ACKNOWLEDGEMENTS

Thanks for the support from the College of Science and Technology Research Project of Hebei Provincial, China (ZD2018044).

References

1. B.C.H. Steele and A. Heinzl, *Nature.*, 6861 (2001) 345-352.
2. H. Zhang and P.K. Shen, *Chem. Rev.*, 112(2012) 2780-2832.
3. H. Zhang, T. Zhang, J. Wang, F. Pei, Y. He and J. Liu, *Fuel Cells.*, 13(2013) 1155-1165.
4. J. Wang, X. Yue, Z. Zhang, Z. Yang, Y. Li, H. Zhang, X. Yang, H. Wu and Z. Jiang, *Adv. Funct. Mater.*, 22(2012) 4539-4546.
5. J. Zheng, J. Wang, S. Zhang, T. Yuan and H. Yang, *J. Power Sources.*, 245(2014) 1005-1013.
6. H. Xie, D. Liu, X. Xiang, C. Zhu and L. Wang, *J. Mater Sci.*, 51 (2016) 7119-7129.
7. H. Zhang, C. Ma, J. Wang, X. Wang, H. Bai and J. Liu, *Int. J. Hydrogen. Energy.*, 39 (2014) 974-986.
8. H. Xie, D. Wang, D. Tao and L. Wang, *J. Power Sources.*, 262 (2014) 328-337.
9. K. Kim, J. Bae, M.Y. Lim, P. Heo, S.W. Choi, H.H. Kwon and J.C. Lee, *J. Membrane Sci.*, 525 (2017) 125-134.
10. W.L. Harrison, M.A. Hickner, Y.S. Kim and J.E. Mcgrath, *Fuel Cells.*, 5 (2005) 201-212.
11. T. Ko, K. Kim, S.K. Kim and J.C. Lee, *Polymer.*, 71(2015) 70-81.
12. G. He, Z. Li, J. Zhao, S. Wang, H. Wu, M.D. Guiver and Z. Jiang, *Adv. Mater.*, 27(2015) 5280-5295.
13. H. F. Lee, B. Britton, Y. C. Huang, T. J. Peckham, Y. Y. Hsu, Y. C. Tseng, P. C. Huang, C. C. Lee, M. Y. Chang and S. Holdcroft, *J. Mater Sci.*, 51 (2016) 1-17.
14. M. L. Einsla, S.K. Yu, M. Hawley, H.S. Lee, J.E. Mcgrath, B. Liu, M.D. Guiver and B.S. Pivovar,

- Chem. Mater.*, 20 (2008) 5636-5642.
15. N. Li, C. Wang, S.Y. Lee, C.H. Park, Y.M. Lee and M.D. Guiver, *Angew. Chem. Int. Edit.*, 123 (2011) 9324-9327.
 16. Y. Yao, Z. Lin, Y. Li, M. Alcoutlabi, H. Hamouda and X. Zhang, *Adv. Energy. Mater.*, 1 (2011) 1133-1140.
 17. G. He, C. Chang, M. Xu, S. Hu, L. Li, J. Zhao, Z. Li, Z. Li, Y. Yin and M. Gang, *Adv. Funct. Mater.*, 25 (2016) 7502-7511.
 18. W. Zhou, J. Xiao, Y. Chen, R. Zeng, S. Xiao, H. Nie, F. Li and C. Song, *Polym. Advan. Technol.*, 22 (2011) 1747-1752.
 19. G. He, J. Zhao, S. Hu, L. Li, Z. Li, Y. Li, Z. Li, H. Wu, X. Yang and Z. Jiang, *Acs Appl. Mater. Inter.*, 6 (2014) 15291.
 20. G. He, M. Xu, J. Zhao, S. Jiang, S. Wang, Z. Li, X. He, T. Huang, M. Cao and H. Wu, *Adv. Mater.*, 29 (2017) 1-8.
 21. L. Xin, S. He, S. Ge, H. Jia, Z. Shi, S. Liu, L. Zhang, J. Lin and S. Nazarenko, *J. Membrane Sci.*, 504 (2016) 206-219.
 22. L. Liu, Y. Wan, Y. Xie, R. Zhai, B. Zhang and J. Liu, *Chem. Eng. J.*, 187 (2012) 210-216.
 23. B. Huang, M. Liu, Z. Long, Y. Shen and C. Zhou, *Mater Sci Eng C Mater Biol Appl.*, 70 (2017) 303-310.
 24. D.G. Shchukin, G.B. Sukhorukov, R.R. Price and Y.M. Lvov, *Small.*, 1 (2005) 510-513.
 25. M. Liu, B. Guo, M. Du, X. Cai and D. Jia, *Nanotechnology.*, 18 (2007) 455703.
 26. H. Bai, H. Zhang, Y. He, J. Liu, B. Zhang and J. Wang, *J. Membrane Sci.*, 454 (2014) 220-232.
 27. U.G. Wegst, H. Bai, E. Saiz, A.P. Tomsia and R.O. Ritchie, *Nat. Mater.*, 14 (2015) 23-36.
 28. L. Cao, X. He, Z. Jiang, X. Li, Y. Li, Y. Ren, L. Yang and H. Wu, *Chem. Soc. Rev.*, 46 (2017) 6725.
 29. P. Joonghyuk, K. Hae Koo, R. Jeongeun, A. Sungsook, L.S. Joon and H. Ildoo, *Plant Cell Physiol.*, 56 (2015) 520-531.
 30. M. Sharma, M. Yi, H. Dong, H. Qin, E. Peterson, D.D. Busath, H.X. Zhou and T.A. Cross, *Science.*, 330 (2010) 509-512.
 31. L.E. Cheruzel, M.S. Pometun, M.R. Cecil, M.S. Mashuta, R.J. Wittebort and R.M. Buchanan, *Angew. Chem. Int. Edit.*, 42 (2003) 5452-5455.
 32. Z. Bai, M.F. Durstock and T.D. Dang, *J. Membrane Sci.*, 281 (2006) 508-516.
 33. J. Pan, H. Yao, L. Xu, H. Ou, P. Huo, X. Li and Y. Yan, *J Phys Chem C.*, 115 (2011) 5440-5449.
 34. M. Yamada and I. Honma, *Angew. Chem. Int. Edit.*, 43 (2004) 3688-3691.
 35. J. Dang, L. Zhao, J. Zhang, J. Liu and J. Wang, *J. Membrane Sci.*, 545 (2018) 88-98.
 36. K.B. Wiles, F. Wang and J.E. Mcgrath, *J Polym Sci Pol Chem.*, 43 (2005) 2964-2976.
 37. W.L. Harrison, W. Feng, J.B. Mecham, V.A. Bhanu, M. Hill, S.K. Yu and J.E. Mcgrath, *J Polym Sci Pol Chem.*, 41 (2003) 2264-2276.
 38. J. Wang, Y. He, L. Zhao, Y. Li, S. Cao, B. Zhang and H. Zhang, *J. Membrane Sci.*, 482 (2015) 1-12.
 39. J. Wang, Z. Zhang, X. Yue, L. Nie, G. He, H. Wu and Z. Jiang, *J. Mater Chem A.*, 1 (2013) 2267-2277.
 40. Y. Yin, H. Wang, L. Cao, Z. Li, Z. Li, M. Gang, C. Wang, H. Wu, Z. Jiang and P. Zhang, *Electrochim. Acta.*, 203 (2016) 178-188.
 41. S.J. Peighamardoust, S. Rowshanzamir, M.G. Hosseini and M. Yazdanpour, *Int. J. Hydrogen Energ.*, 36 (2011) 10940-10957.
 42. J. Jaafar, A.F. Ismail, T. Matsuura and K. Nagai, *J. Membrane Sci.*, 382 (2011) 202-211.
 43. G. He, Y. Li, Z. Li, L. Nie, H. Wu, X. Yang, Y. Zhao and Z. Jiang, *J. Power Sources.*, 248 (2014) 951-961.
 44. L. Nie, G. He, H. Dong and Z. Jiang, *J. Power Sources.*, 213 (2012) 1-9.
 45. Y. He, J. Wang, H. Zhang, T. Zhang, B. Zhang, S. Cao and J. Liu, *J. Mater Chem A.*, 2 (2014) 9548-9558.
 46. R. Jin, Y. Li, W. Xing, X. Qiu, X. Ji and L. Gao, *Polym. Advan. Technol.*, 23 (2012) 31-37.

47. Y. Yin, T. Xu, G. He, Z. Jiang and H. Wu, *J. Power Sources.*, 276 (2015) 271-278.
48. J. Wang, H. Zhang, X. Yang, S. Jiang, W. Lv, Z. Jiang and S.Z. Qiao, *Adv. Funct. Mater.*, 21 (2015) 971-978.
49. B. Zhang, Y. Cao, S. Jiang, Z. Li, G. He and H. Wu, *J. Membrane Sci.*, 518 (2016) 243-253.
50. F. Bu, Y. Zhang, L. Hong, W. Zhao, D. Li, J. Li, H. Na and C. Zhao, *J. Membrane Sci.*, 545(2018) 167-175.
51. Y. Wei, Y. Shang, H. Zhang, X. Li, B. Liu, Y. Men, M. Zhang and W. Hu, *Appl. Surf. Sci.*, 416 (2017) 996-1006.
52. P.N. Venkatesan and S. Dharmalingam, *J. Membrane Sci.*, 435 (2013) 92-98.
53. J. Venkatesan, B. Ryu, P.N. Sudha and S.K. Kim, *Int. J. Biol. Macromol.*, 50 (2012) 393-402.
54. C. Ni, Y. Wei, Q. Zhao, B. Liu, Z. Sun, Y. Gu, M. Zhang and W. Hu, *Appl Surf Sci.*, 434 (2018) 163-175.
55. X. Xu, R. Li, C. Tang, H. Wang, X. Zhuang, Y. Liu, W. Kang and Shi L, *Carbohydr Polym.*, 184 (2018) 299-306.
56. C. Jin, X. Zhu, S. Zhang and S. Li, *Polymer.*, 148 (2018) 269-277.
57. M. K. Ahna, S. B. Lee, C. M. Mina, Y. G. Yu, J. Jang, M. Y. Gima and J. S. Lee, *J. Membrane Sci.*, 523 (2017) 480-486.
58. J. Li, S. Wang, J. Xu, L. Xu, F. Liu, X. Tian and Z. Wang, *J. Membrane Sci.*, 529 (2017) 243-251.
59. Y. Wei, Y. Shang, C. Ni, H. Zhang, X. Li, B. Liu, Y. Men, M. Zhang and W. Hu, *Appl Surf Sci.*, 416 (2017) 996-1006.
60. Z. Wu, Y. Tang, D. Sun, S. Zhang, Y. Xu, H. Wei and C. Gong, *Polymer.*, 123 (2017) 21-29.
61. B. G. Choi, Y. S. Huh, Y. C. Park, D. H. Jung, W. H. Hong and H. Park, *Carbon.*, 50 (2012) 5395-5402.
62. C. Ni, Y. Wei, Q. Hu, X. Li, B. Liu, Q. Zhao, M. Zhang, Y. Li and W. Hu, *Solid State Ionics.*, 297 (2016) 29-35.
63. C. Li, Y. Zhang, X. Liu, J. Dong, J. Wang, Z. Yang and H. Cheng, *J. Mater Sci.*, 53 (2017) 5501-5510
64. R. Chen, J. Jin, S. Yang and G. Li, *J. Mater Sci.*, 52 (2016) 1-11.
65. K. Oha, B. Son, J. Sanetuntikul and S. Shanmugam, *J. Membrane Sci.*, 541 (2017) 386-392.
66. H. Q. Li, X. J. Liu, J. Xu, D. Xu, H. Ni, S. Wang and Z. Wang, *J. Membrane Sci.*, 509 (2016) 173-181.
67. Y. Wei, X. Li, Q. Hu, C. Ni, B. Liu, M. Zhang, H. Zhang and W. Hu, *Rsc Adv.*, 6 (2016) 65072-65080.
68. G. He, J. Zhao, S. Hu, L. Li, Z. Li, Y. Li, Z. Li, H. Wu, X. Yang and Z. Jiang, *Acs Appl Mater Inter.*, 6 (2014) 15291-15301.
69. M. Eikerling, A. A. Kornyshev, A. M. Kuznetsov, A. J. Ulstrup and S. Walbran, *J. Phys. Chem. B.*, 105 (2001) 3646-3662.
70. Mohammed, D. Pines, E.T.J. Nibbering and E. Pines, *Angew. Chem. Int. Edit.*, 119 (2007) 1480-1483.